CrystEngComm

Accepted Manuscript

ROYAL SOCIETY OF CHEMISTRY

www.rsc.org/crystengcomm

Revised Manuscript ID: CE-ART-03-2015-000526-R2

In situ high temperature X-ray diffraction, transmission electron microscopy and theoretical modeling for the formation of WO_3 crystallites

Suman Pokhrel[1], Johannes Birkenstock,[2] Arezoo Dianat[3,4], Janina Zimmermann[3,5], Marco Schowalter[6], Andreas Rosenauer[6,7], Lucio Colombi Ciacchi[3,7], L. Mädler[1,7*]

[1]Foundation Institute of Materials Science (IWT), Department of Production Engineering, University of Bremen, Germany
[2]Central Laboratory for Crystallography and Applied Materials, University of Bremen, Germany
[3]Hybrid Materials Interfaces Group, Department of Production Engineering and Bremen Center for Computational Materials Science, University of Bremen, Germany
[4]Institute for Materials Science, University of Dresden, Germany
[5]Fraunhofer Society Headquarter, Munich, Germany
[6]Institute of Solid State Physics, University of Bremen, Germany
[7]MAPEX Center for Materials and Processes, University of Bremen, Germany

Abstract

We study the transformation that WO_3 nanoparticles produced by Flame Spray Pyrolysis undergo when subjected to heating and cooling cycles by means of accurate *in-situ* XRD and HRTEM investigations supported by atomistic modeling at the level of Density Functional Theory. As-deposited particles, initially in the monoclinic phase, reversibly transform into the high-temperature orthogonal and tetragonal phases (and vice versa) irrespective of the direction of the temperature gradient. However, upon heating the particles experience an irreversible change of morphology as a consequence of evaporation/reprecipitation processes leading to the formation of larger particles, some of which are elongated (aspect ratios of up to 3:1) along various crystallographic directions of the tetragonal unit cell. On the basis of the results of extensive ab-initio thermodynamic calculations of surface energies and first-principles Molecular Dynamics simulations of the growth process, we rationalize these findings in terms of different surface stabilities and reactivities towards gas-phase deposition of molecular WO_3 presented by the nanocrystal facets.

**Corresponding author*: lmaedler@iwt.uni-bremen.de (Lutz Mädler)

Revised Manuscript ID: CE-ART-03-2015-000526-R2

1. Introduction

Tungsten trioxide, WO_3, is an important wide-band semiconductor material with a broad range of applications in electrochemical cells, gas sensors and display devices.[1] Recently, numerous synthetic routes have been developed for the preparation of WO_3, including flame spray pyrolysis (FSP), surfactant tailored synthesis, template directed/free synthesis, solution-based colloidal approach, chemical vapor deposition/thermal deposition and hydrothermal synthesis.[2] Many of these techniques produce WO_3 nanoparticles, which can be employed in this form or converted, *via* appropriate thermal treatments, into elongated nanostructures such as rods or wires. The latter are specifically important for diverse applications in electrochromic devices,[3] display technologies[1f] (since the reflectivity of the rods can be changed by adjusting their orientation within an electric field), fuel cells, and other optical or electronic devices.[4] Tailoring the physical properties of WO_3 nanostructures can be achieved by accurate control of their morphology and crystallographic ordering, exploiting the variety of phases stable at different temperatures. Of technological importance is especially the monoclinic γ-phase, stable at room temperature, and the tetragonal α-phase, stable at high temperatures and often found in the form of elongated particles with high aspect ratios.

In a well-known technique for the production of WO_3 nanowires or rods, an oxygen flow is directed over a hot tungsten filament causing the formation of gaseous tungsten oxide species (such as WO_2 or WO_3).[5] When the gas products are collected onto substrates maintained at temperatures below the decomposition temperature of bulk WO_3, they condense according to nucleation-and-growth mechanisms that can be controlled by the substrate temperature. In general, for high-melting, yet sublimating metal oxides like WO_3, solid/gas transformations (e.g evaporation/re-precipitation mechanisms) may be employed for the growth of different

Revised Manuscript ID: CE-ART-03-2015-000526-R2

morphological WO3 nanoparticles with different crystal symmetries.[6] In this context, the detailed knowledge of the growth mechanism of WO_3 is important to tailor the fabrication process for various commercial products.[7] In order to obtain an in-depth understanding of the correlation between processing/post-processing conditions, we demonstrate the associated crystallographic phase transformations and the resulting nanocrystal habitus during heating and cooling cycles. To this aim we perform a precise *in-situ* X-ray diffraction (XRD) and high-resolution transmission electron microscopy (HRTEM) analysis combined with quantum mechanical atomistic modeling at the level of Density Functional Theory (DFT).

Our study reveals that *crystallographic* transformations between all stable WO_3 phases upon temperature changes are reversible, yet an irreversible change of particle *morphology* takes place during a heating/cooling cycle of FSP-produced nanoparticles. Namely, the latter recrystallized into larger particles due to a combination of particle-particle agglomeration and evaporation/re-precipitation of gaseous tungsten oxides. Some of the particles are elongated with aspect ratios of up to 3:1. For the latter, by accurate analysis of HRTEM data, we reveal several preferred growth directions and correlate them with the surface energy values computed within an ab-initio thermodynamics framework. We highlight the importance of taking into account the correct oxygen termination of the surfaces, and unveil atomistic details of the growth process by means of ab-initio molecular dynamics simulations.

2. Experimental

2.1. X-ray diffraction

For all X-ray diffraction measurements we used a PANalytical X'Pert MPD Pro system with Ni-filtered Cu $K_{\alpha 1-\alpha 2}$ radiation. A fixed divergence of ¼° was applied together with primary and

Revised Manuscript ID: CE-ART-03-2015-000526-R2

secondary Soller slits of 0.04 and 0.0175 rad, respectively, to minimize over irradiation and asymmetry effects. Intensities were recorded by a PANalytical X'Celerator detector with 127 channels of 0.01671° aperture each, in continuous scanning mode in the range of 15-140°2θ and with an integration step width of 0.0334°2θ. The measuring time step was nominally 170 s, to be divided by 127 channels to yield an effective measuring time of 1.34 s per 0.0334°2θ. For the *in-situ* recordings, a ceramic sample holder (α-Al_2O_3) with a diameter of 15 mm and a depth 0.8 mm was placed in a high-temperature chamber HTK 1200N (Anton Paar Co.). In-house calibration measurements with the chamber yielded temperature variations of less than 2°C within the sample and a systematic offset of -8 °C within the range of ~100 to ~600 °C. During the series of *in-situ* high-temperature measurements (45 minutes per scan at each constant temperature) the sample was equilibrated for 10 minutes before each measurement, applying a heating rate of 20 °C/min between them.

2.2. Synthesis and microscopy

The WO_3 nanopowders were prepared with the FSP process described elsewhere [7]. In short, the tungsten hexacarbonyl (99.9% pure, Strem) precursor was dissolved in tetrahydrofuran (THF, 99.95%, Strem) and delivered (5 mL/min) into the FSP reactor. The dispersed precursor solution was combusted using CH_4 and O_2 (1.5 L/min, 3.2 L/min) to obtain fine particles. These as-prepared particles were dispersed in absolute ethanol and sonicated for one hour. A drop of this suspension was placed on a copper grid coated with carbon film followed by drying the grid at ambient conditions before scanning the images. The TEM specimens were investigated with a FEI Titan 80/300 microscope equipped with a Cs corrector for the objective lens, a Fischione high angle annular dark field detector (HAADF) and a GATAN post-column imaging filter. For all studies the microscope was operated at 300 kV. The *in-situ* TEM imaging was performed with

Revised Manuscript ID: CE-ART-03-2015-000526-R2

a single-tilt Gatan heating holder in built within the Titan 80/300 instrument capable of achieving a maximum temperature of 1100 °C. Our *in-situ* heating experiments were performed up to 950 °C on grids made with a copper mesh. The images (HRTEM, LRTEM, and SAED) were recorded at 50°C temperature intervals. A heating rate of 20°C/min was employed for the measurements. The d_{TEM} of the particles at room temperature were measured on an ensemble of 50 particles along and perpendicular to their axes where the average diameter of a single particle was derived.

2.3. Density Functional Theory modeling

Our static DFT calculations of surface energies were performed according to the Projector Augmented Waves (PAW) method using the PBE[54] generalized gradient approximation (GGA) for the exchange-correlation functional as implemented in the Vienna ab initio simulation package (VASP).[8] The wave functions were expanded in plane waves up to a kinetic energy cut-off of 600 eV for bulk and 400 eV for surface calculations. Integration in the first Brillouin zone was performed using Monkhorst-Pack grids with a 4x4x4(1) k-point mesh in the crystal unit cells for bulk (surface) calculations. For each considered phase, the shape and volume of the unit cell as well as the internal atomic coordinates were fully optimized until all force components were less than 10^{-3} eV/Å^2. The molecular dynamics (MD) simulations were performed with a similar setup (Plane Waves, PAW, PW91 GGA functional, 540 eV kinetic energy cutoff) using the Car-Parrinello method as implemented in the Lautrec code. The generated PAW datasets treated 14 explicit valence electrons for tungsten and 6 for oxygen, including 3,2,0 (W) and 2,2,0 (O) projectors for the s,p,d angular momentum components. The α-WO_3 (001) and (100) surfaces were modeled using slabs of a thickness of about 8 and 9 Å, corresponding to 3 and 4 atomic layers in the respective directions, with surface unit cells of areas 10.6x10.6 and 11.8x10.6 Å^2

Revised Manuscript ID: CE-ART-03-2015-000526-R2

including 8 and 6 W atoms, respectively. The surface unit cells were sampled at the (0.25, 0.25) point of the Brillouin zone. The WO-terminated slabs were separated by vacuum gaps of at least 15 Å thickness, providing enough free space to model the adsorption of WO_3 gas molecules.

3. Results

3.1. X-ray diffraction

We start our investigation with the *in-situ* examination of a pristine sample of WO_3 prepared by FSP by means of high-temperature diffraction during a coherent heating and cooling cycle, running from 25 °C to 800°C and back to RT. The series of measurements are presented in Fig. 1 (a) and (b) showing a continuous interpolated image[9] with explicit diffraction patterns superimposed at selected temperatures.

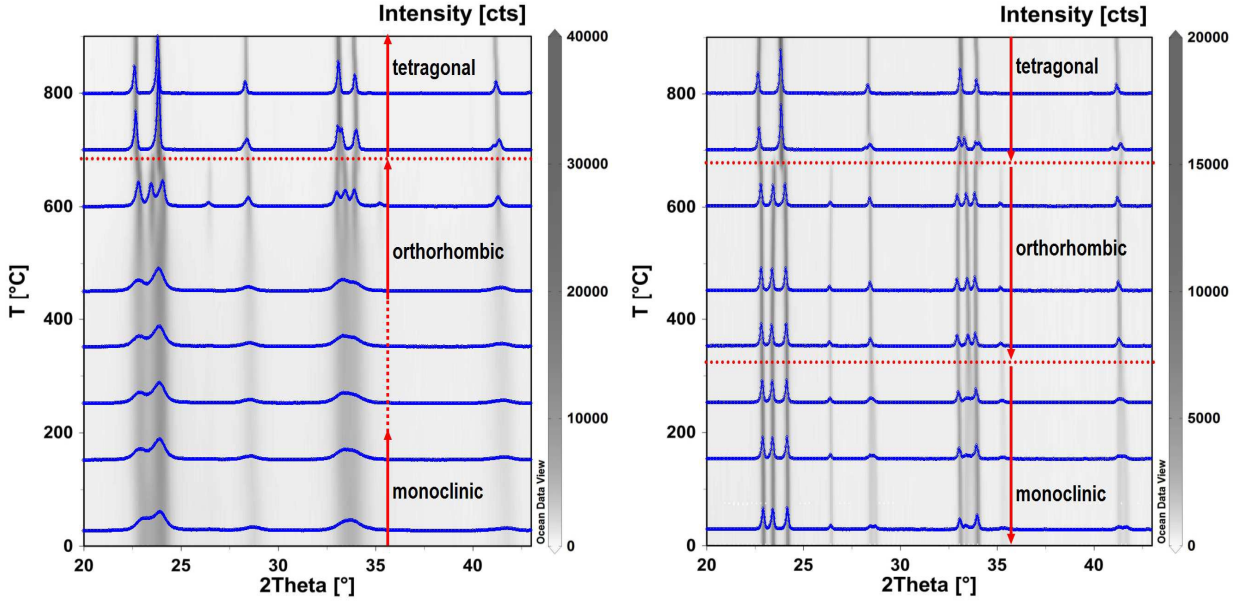

Fig. 1 XRD patterns of WO_3 nanoparticles plotted by ODV (ocean data view) observed *in-situ* from room temperature to 800° C on (a) heating (b) cooling. The structural transformations can be seen very clearly from the plot.

At room temperature, broad reflections typically characterize the as-synthesized WO_3 nanoparticles. During heating, a significant reduction in the broadness occurs between 450 and 600 °C, which can be associated with crystal growth. In the temperature range 600-700 °C, two

Revised Manuscript ID: CE-ART-03-2015-000526-R2

groups of main reflections at about 23°2θ and 34°2θ become well resolved. At 700 °C a very distinct transformation into a different phase is observed, characterized by narrow, well resolved XRD peaks. Upon cooling, a similar sequence was observed in reversed order. However, due to the improved resolution of the reflections, two phase transformations are now clearly observed, one at about 675 °C when a new peak appears at 26.5° 2θ, and a second one between 350 and 300 °C. The latter is identified by the splitting of some of the peaks, e.g. at 29 or 42°2θ (Fig. 1).

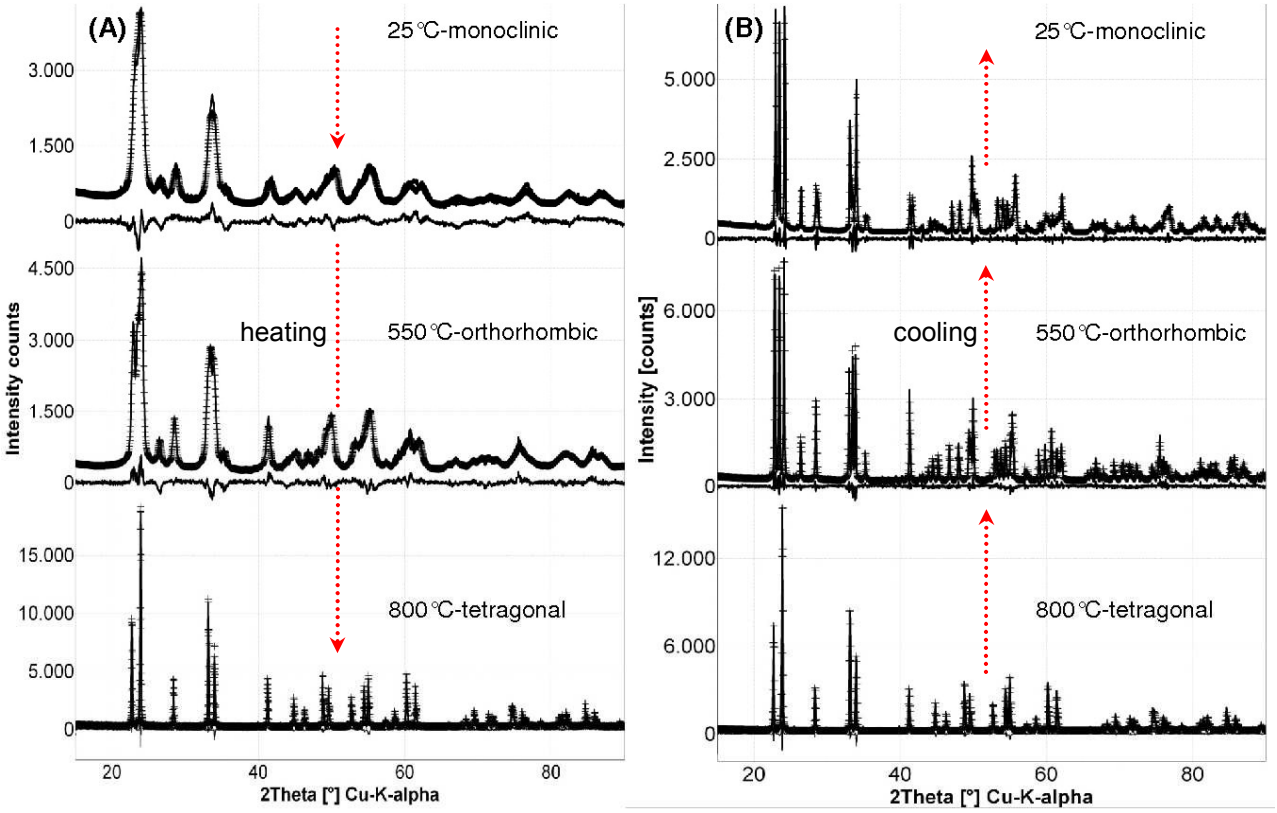

Fig. 2 Representative Rietveld fittings of the WO_3 (A) heating patterns from 25-800°C and (B) cooling patterns from 800-25°C showing reversible structural transformation in the order monoclinic – orthorhombic – tetragonal phase and vice versa during cooling.

Rietveld analyses of selected high temperature X-ray plots are performed using the BRASS program [10] and presented in Fig. 2 (A) and (B) for the heating and cooling ramps, respectively. The cooling data show with clarity the expected sequence of WO_3 phases.[11] Namely: a tetragonal phase with space group P 4/n c c (ICSD # 50733) at the highest temperatures, an orthorhombic

Revised Manuscript ID: CE-ART-03-2015-000526-R2

phase with space group P c n b (ICSD # 50728) at intermediate temperature and a monoclinic phase with space group P 2_1/n (ICSD # 80056) at room temperature (see Tab. 2 and ESI †).

For the initial heating series the analysis is rather difficult due to non-Bragg scattering phenomena together with extremely broadened reflections. As a result, the monoclinic and the orthorhombic phase are difficult to distinguish (see Fig. 1 and 2): the typical splitting of reflections in the monoclinic phase is not clearly recognizable due to the overlap of reflections caused by the rather strong peak broadening typical for such samples. However, it is still possible to obtain reasonable fits using the monoclinic model at room temperature and the orthorhombic model above ~400°C. From the Rietveld analyses, we can estimate the characteristic sizes of the particles from the peak broadness (assuming negligible contributions from crystal disorder). As reported in Fig. 2, the FSP synthesized monoclinic primary particles (crystallite size d_{XRD} ~7 nm) grow progressively during heating through the first monoclinic-orthorhombic transformation (d_{XRD} ~15 nm). At about 700°C, a sudden increase of the particle size occurs when the orthorhombic-tetragonal (O-T) phase transformation occurs (d_{XRD} ~90 nm). Upon cooling, all phases present rather large characteristic sizes, indicating that an irreversible morphology change takes place during heating while the particles undergo the O-T transition. The particle morphologies during the thermal treatment are investigated by means of HRTEM imaging in the next section.

Tab.1 Rietveld analyses of selected temperature XRD patterns from the *in-situ* high temperature x-ray diffraction experiment on WO_3 sample and comparison to those of the respective database entries applied as starting models for the Rietveld analyses.

T [°C]	Fit	Phase (space group)	Lattice Parameters [Å], Vol.[Å³]	ICSD entry	PDF entry	[R_{wp}, R_p, R'_p, R_B]* / Crystal size (nm)]

Revised Manuscript ID: CE-ART-03-2015-000526-R2

25	R	M (P 2_1/n)	**Heating** WO_3 P 2_1/n a = 7.378(2) b = 7.484(2) c = 7.678(2) β = 90.68(4) V =424.0(3) **Cooling** a = 7.3056(2) b = 7.5348(2) c = 7.6952(2) β = 90.757(4) V =423.45(3)	80056 P2_1/n a = 7.30084(7) b = 7.53889(7) c = 7.68962(8) β = 90.892(1) V = 423.19	75-2072 a = 7.3013 b = 7.5389 c = 7.6893 β = 90.8930 V = 423.19	8.8, 7.7, 19.3, 11.3 7.0(2) nm 9.5, 6.9, 15.4, 3.4 52(1) nm
550	R	O (Pbcn)	**Heating** a = 7.388(1) b = 7.757(1) c = 7.544(1) V = 432.4(1) **Cooling** a = 7.3683(1) b = 7.7673(1) c = 7.5728(1) V =433.41(1)	50730 a = 7.3612(2) b = 7.5739(2) c = 7.7620(3) V = 432.75	01-089-4479 a = 7.3612 b = 7.5739 c = 7.7620 V = 432.75	8.0, 6.2, 11.9, 6.1/ 15.1(4) nm 8.1, 6.3, 13.6, 7.2 76(9) nm
800	R	T (P 4/n c c)	**Heating** a = 5.2801(5) c = 7.8497(1) V= 218.85(4) **Cooling** a = 5.2801(6) c = 7.8489(1) V= 218.83(5)	50732 a = 5.2759(1) c = 7.8462(3) V = 218.4	01-089-4481 a = 5.2759 c = 7.8462 V = 218.4	9.8, 7.7, 17.3, 10.3 89 (1) nm 10.4, 8.1, 19.2, 10.0 86(1) nm

**Rietveld agreement indices related to the whole profile: R_{wp}-weighted profile, R_p-Profile, R'_p-background corrected profile, R_B-Bragg profile*

3.2. Transmission electron microscopy

The morphologies of the nanoparticles during a heating/cooling cycle are investigated by *in-situ* HRTEM imaging. Fig. 3 shows images of the nanoparticle aggregates, their high-resolution atomic structure and the associated selected area electron diffraction (SAED) patterns at the three

Revised Manuscript ID: CE-ART-03-2015-000526-R2

different temperature regimes where structural transformations have been observed in the XRD investigation.

At room temperature, the as-synthesized primary particles have an average size d_{TEM} of about 8-10 nm (Fig. 3a), which is in good agreement with the size estimated from the Rietveld analysis (d_{XRD} = 7.0 nm) and the one determined by BET gas adsorption (d_{BET} = 9.1 nm).[2e] The HRTEM image (Fig. 3b) reveals well-developed lattice fringes with a spacing of about 3.880(2) Å, which is in reasonable agreement with half of the distance along the c vector of the monoclinic cell as obtained from XRD (a = 7.38 Å, b = 7.48 Å, c = 7.68 Å, β = 90.7°, see Tab. 1). The lattice distance of 3.880(2) Å is derived by choosing at least 10 crystalline particles having well-developed fringes. The particles are magnified and the fringes measured at least at 5 different spots for each particle. Indeed, the SAED pattern of the nanomaterial presents the same monoclinic symmetry [Fig. 3c] oriented with respect to the electron beam following the basic unit cell vectors [1 0 0], [0 1 0] or [0 0 1].

The morphology of the particles heated at 450°C (Fig. 3d) is similar to the one at room temperature, but their characteristic size increases to d_{TEM}= 15-18 nm. Notably, a further size increase to 20-25 nm is found at 600°C (image not shown). These values are again in good agreement with the XRD data collected at 550°C (d_{XRD} = 15.1 nm), and indicate that the particles progressively enlarge when they are heated. The HRTEM image and SAED pattern (Fig. 3 e,f) are fully consistent with the expected orthorhombic symmetry[12] (a = 7.39 Å, b = 7.76 Å, c = 7.54 Å from XRD, see Tab. 1), identifying normal distances of 0.3828(2) Å and 0.3815(3) Å nm corresponding to ½ the distances of (001) and (010) planes and thus to second order diffractions (002) and (020), respectively. We note that the lattice distances for the monoclinic phase and orthorhombic phase are quite similar, so that the phases can only be discriminated due to the

Revised Manuscript ID: CE-ART-03-2015-000526-R2

splitting of the XRD-peak positions at around 29 and 42° (2θ) in case of the monoclinic phase. The unit cell relationships between the phases will be discussed later in section 3.3.

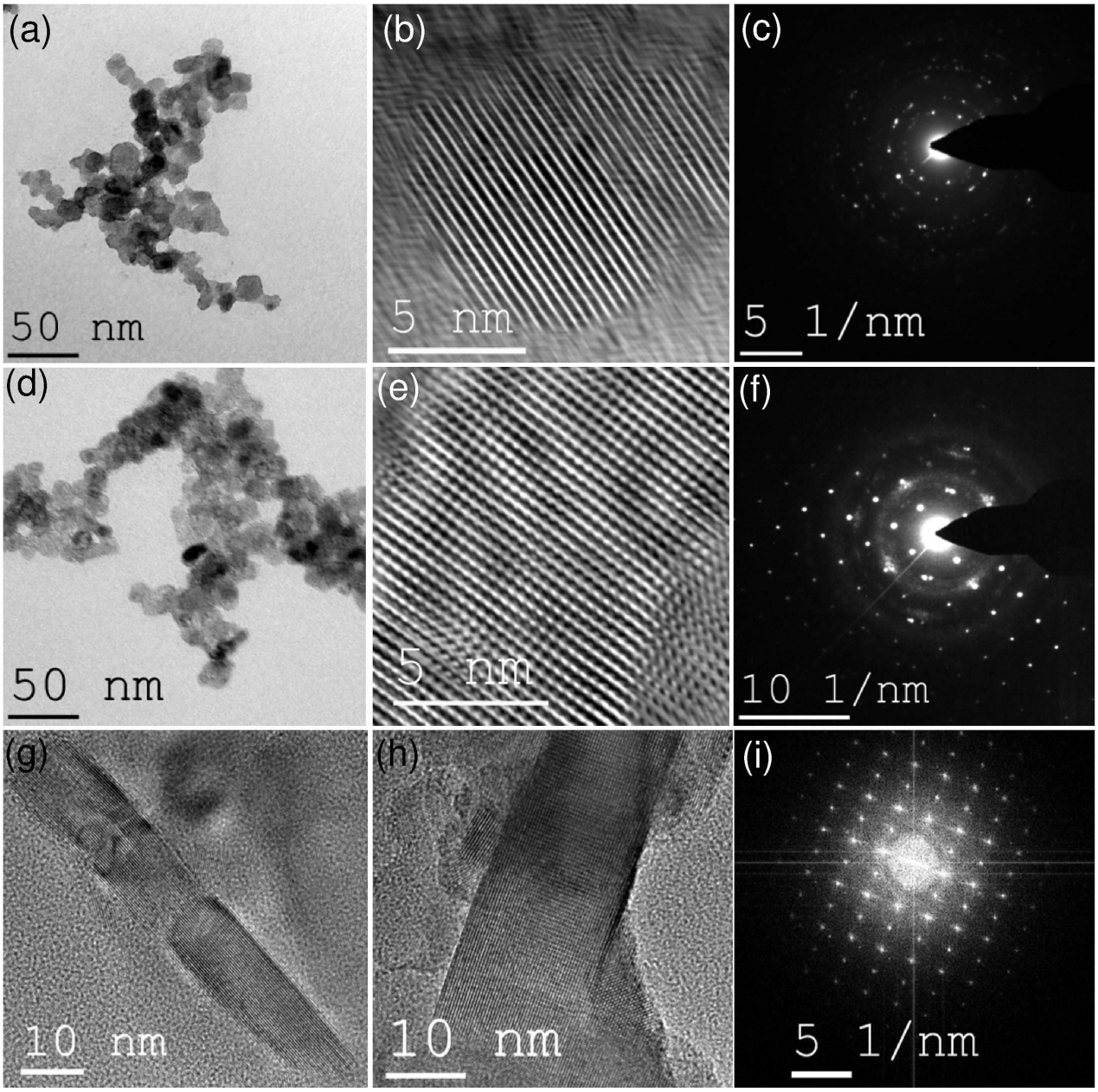

Fig. 3 *In-situ* TEM investigation of WO_3 nanoparticles. First row (a), (b) and (c): Overview, HRTEM of a single particle and SAED patterns of particles at room temperature; second row (d), (e) and (f): Overview, HRTEM of a single particle and SAED patterns of the particle at 450°C. (g), (h) TEM images at room temperature of elongated particles obtained after heating the sample in the Al_2O_3 crucible in the XRD instrument at 1000°C (i) FFT filtered spot patterns of the particle obtained from elongated particle shown in (h).

Revised Manuscript ID: CE-ART-03-2015-000526-R2

Upon further heating, the morphology of the WO_3 particles remains unchanged up to the onset of the O-T phase transformation (~700°C). At this point the particles visibly form larger aggregates, while they also presumably sublimate with formation of gaseous WO_3, as suggested by the evident mobility of the particles on the copper grid. With increasing temperatures (800-950°C), these aggregates recrystallize into larger particles, some of which are elongated with aspect ratios of up to 3:1. The XRD data undoubtedly indicate that a transition to the tetragonal alpha-WO_3 phase takes place at these temperatures. This is accompanied by a sudden increase of crystallite size (d_{XRD} = 90 nm) compatible with the formation of larger crystals and few elongated particles (see Fig. 3 g-i).

To exclude any spurious effects on the observed transformation due to the Cu support used in the TEM investigations discussed so far, we also performed a high temperature XRD investigation of sample deposited on a ceramic sample holder (α-Al_2O_3). After the treatment at 1000°C, the samples were investigated with HRTEM, but now at room temperature only. Also in this case, we find that some particles were elongated. Namely, the elongated particles had a length of about 100-150 nm and presented a very clear crystalline structure (Fig. 3 g). It must be stressed that the particles formed at high temperatures have *tetragonal* symmetry, but upon cooling they undergo a tetragonal-orthorhombic-monoclinic transformation series. Therefore, in order to understand the orientation of the elongated particles in the high-temperature tetragonal phase it is necessary to summarize the relationships between the three crystallographic systems.

3.3. Relations between unit cells and growth directions of the elongated crystals

The relations between the unit cells of three systems (monoclinic $P2_1/n$; orthorhombic Pbcn; tetragonal P4/ncc) are drawn schematically in Fig. 4 (m=monoclinic, o=orthorhombic, t=tetragonal). Apart from the small variations of their length, the cell vectors are related as:

Revised Manuscript ID: CE-ART-03-2015-000526-R2

$\mathbf{a}_m \approx \mathbf{a}_o \approx (\mathbf{a}_t - \mathbf{b}_t)$; $\mathbf{b}_m \approx \mathbf{c}_o \approx (\mathbf{a}_t + \mathbf{b}_t)$; $\mathbf{c}_m \approx \mathbf{b}_o \approx \mathbf{c}_t$.

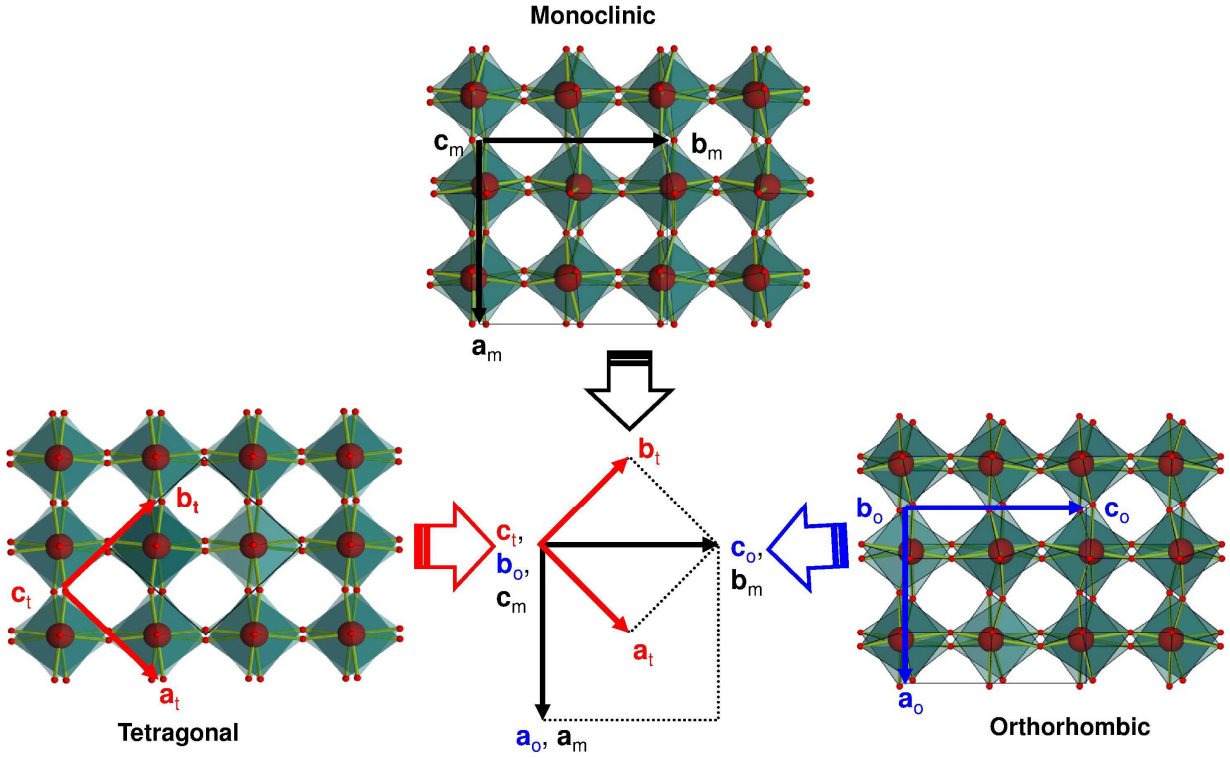

Fig. 4 Structural relations between the three crystal phases (monoclinic-orthorhombic-tetragonal) observed during *in-situ* heat treatment from room temperature to 950°C.

In order to establish the crystallographic directions of the long and the short directions of the elongated particles we derived the lattice spacings from high resolution TEM images and – where available – from the corresponding Fourier-Transformed images. Two of the representative TEM images showing different growth directions are presented in Fig. 5 a, b. Considering the direct and reciprocal (Fourier-Transformed) HRTEM images of the elongated particle in Fig. 3h (crystallographic investigation shown in Fig. 5a), after cooling to room temperature, the lattice distance along the long direction is 0.26(3) nm. In the same direction, the shortest reciprocal distance spacing d* is 1.9 nm^{-1}. These values reasonably correspond to the lattice spacing of (220) of the monoclinic phase, since d_{220}=0.262 nm and d^*_{110}=1.91 nm^{-1}, respectively. In fact, d_{003}=0.258 nm is also very close to 0.26 nm, yet the corresponding

Revised Manuscript ID: CE-ART-03-2015-000526-R2

d^*_{001}=0.130 nm^{-1} does not fit to the observed value of 0.19 nm^{-1}. Thus, we infer that the long direction of the elongated particle should be $[110]_m$, which corresponds to $[100]_t$ in the tetragonal system. For the short direction we determined d=0.37 nm and d*=2.63 nm^{-1}, which correspond reasonably well with d_{002}=0.385 nm and d^*_{002}=2.60 nm^{-1} in the monoclinic system. In fact, d_{200}=0.365 and d_{020}=0.377 nm are even closer to 0.37 nm, yet $[100]_m$ and $[010]_m$ are not approximately perpendicular to $[110]_m$. Thus, together with the above long direction the short direction is inferred to be $[001]_m$, which corresponds to $[001]_t$ in the tetragonal system. In fact there are two more, similar pairs of directions which would also match the observed ones with a similar overall quality. These are 202 (d202 = 0.263 nm, d*101 = 1.90 nm-1) + 020 (d = 0.377 nm; d* = 2.66 nm-1) and furthermore 022 (d022 = 0.269 nm, d*011 = 1.86 nm^{-1}) + 200 (d 0.365 nm, d* = 2.74 nm^{-1}). All these three pairs comply with the observed values within the uncertainties so it is not possible to assign the observation to one of these unequivocally.

For a second particle (Fig. 5b), the long direction presents a d-spacing of 0.385 nm and thus corresponded to $d_{0\,0\,2}$. For the short one the spacing is 0.357 nm corresponding at best to d_{200}=0.365 nm in the monoclinic system. In a further particle, the long and short directions correspond to $d_{2\,0\,0}$ and $d_{0\,2\,0}$, respectively (Fig. 5c).

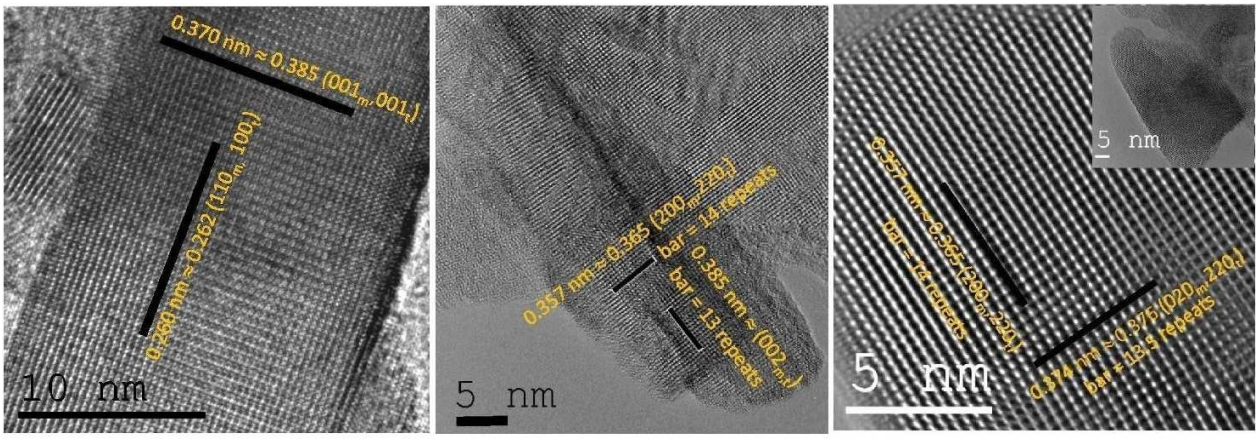

Fig. 5 Representative elongated WO_3 particles and their growth directions. (a) HRTEM images of the elongated particle in Fig. 3h after cooling to room temperature. The lattice spacing of the long direction is 0.26 nm corresponding to $(220)_m$ (and direction $[110]_m$) of the monoclinic phase

Revised Manuscript ID: CE-ART-03-2015-000526-R2

(equivalent to $[100]_t$ in the tetragonal phase). The short direction is $[001]_m$, corresponding to $[001]_t$ in the tetragonal system. (b) In another example, the resulting long direction presents a d-spacing of 0.385 nm corresponding to $d_{0\,0\,2}$, the short distance was 0.357 nm corresponding at best to d_{200} = 0.365. (c) Here the spacing in the long direction is 0.365 nm corresponding to $d_{2\,0\,0}$ while the short direction is 0.376 nm corresponding to $d_{0\,2\,0}$ in the monoclinic system.

3.4. Growth directions in the frame of tungsten oxide research

Elongated crystals have been reported in a number of studies. Depending on the growth conditions, $WO_{2.9}$ prepared by electron-beam induced evaporation [6a] have different morphologies (fibers or rods) with declared tetragonal $[110]_t$ growth elongation direction. In experiments using the gas condensation technique, [13] the selective preparation of WO_3 or $W_{19}O_{55}$ with $[001]_t$ preferential growth direction could be obtained by varying the O_2 partial pressure. Similarly, 2D WO_{3-x} nanowire networks have been synthesized[14] using thermal evaporation of WS_2 in a humid environment. The $WO_{2.9}$ nanowire was reported to be in the tetragonal phase with a $[110]_t$ growth direction. Su *et al.* reported [15] tetragonal $WO_{2.8}$ using plasma arc gas condensation technique with $[001]_t$ growth direction. Mwakikunga *et al* reported the transformation of WO_3 nanospheres into $W_{18}O_{49}$ one dimensional nanostructure through sintering process. The results showed that the as prepared samples were oxygen deficient monoclinic WO_{3-x}. After thermal treatment, the XRD signals in the range of 22–40 (2θ) were assigned to $W_{18}O_{49}$ where $2\theta = 38.12°$ representing [1 0 0] plane. They also reported that the $W_{18}O_{49}$ wires were growing preferentially in the [100] and [102] direction although [102] is not a preferred growth direction.[16] Hot filament thermal deposition technique can also produce slim tetragonal WO_3 nanorods growing in the $[001]_t$ direction[17] or oxygen-deficient tetragonal WO_{3-x}, also growing in the $[001]_t$ direction.[18]

There is some confusion in the literature about deficient and non-deficient phases which has some impact on the growth direction assignment. For instance, Zhao *et al*. assigned the high-temperature P 4/n m m phase to powder patterns of their samples using PDF entry 18-1417 (with low quality mark “blank”) which provides $WO_{2.9}$ as chemical composition. [6a, 14] Yet, the more

Revised Manuscript ID: CE-ART-03-2015-000526-R2

recent and higher rated entries of the P 4/n m m phase declare its composition to be WO_3: 01-72-5863 (medium quality "indexed"), 01-89-8053 (high quality "star"). The related entries in the ICSD file confirm the composition of WO_3. Furthermore, as WO_3 with symmetry P 4/n m m is only stable at high temperatures, it is not comprehensible why this phase should be observed at room temperature at all [see ESI † (both doc and excel file)]. We thus conclude that the above authors in fact did not observe the declared phase with symmetry P 4/n m m but the deficient $WO_{2.9}$ phase with symmetry P $\bar{4}$ 2_1 m. This would also result in a different orientation of the growth direction as that would be [1 0 0] with respect to the P $\bar{4}$ 2_1 m symmetry and not [1 1 0], as assigned with respect to the P 4/n m m symmetry. In summary, while elongated particles show a clearly preferred growth direction in some cases (for instance [100]t in Fig. 3(g,h)), other elongation directions are also possible and seem to depend on the precise preparation conditions. This points towards a combination of both thermodynamic and kinetics effects driving the formation of elongated particles according to evaporation/reprecipitation mechanisms.

Tab. 2 Comparison of structure models reported for WO_3 rods in the literature and in the present investigation. The differences in the calculated XRD patterns of these structures are presented in Fig. 6. *Denotes the WO_3 phases observed in the present investigation [see ESI † (both doc and excel file)].

S. No.	Phase	Space group (# in ITCr)	Lattice parameters & rod direction [uvw]	ICSD No.	Pdf No.	Ref
1.	WO_{3-x}	Tetragonal, P 4/n m m (129)	a=5.30(4) b=5.30(4) c=3.93(3) β=90, [001]	-	18-1417	18
2.	$W_{18}O_{49}$	Monoclinic, P 2/m (10)	a=18.31, b=3.78 c=14.03, β=115.21, [100]	15254	84-1516	16
3.	$W_{18}O_{49}$	Monoclinic, P 2/m (10); after annealing P 2_1/n (13)	a=18.28, b= 3.775, c=13.98 β=115.2, [010] a=7.30(1) b=7.54(1) c=7.69(1) β=90.88(5), [uvw notdetermined]	16080	05-0392; 43-1035	19
4.	WO_3	Monoclinic $P2_1/a$ (14)	a=7.27(2) b=7.501(1) c=3.82(3) β=90.93, [001]	31823	75-2072	6b

Revised Manuscript ID: CE-ART-03-2015-000526-R2

5.	W_3O_8	Orthorhombic, P b a m (55)	a=10.35(5) b=13.99(5) c=3.78(1) β=90,[001]	73720	81-2263	6c
6.	$WO_{2.9}$	Monoclinic $P2_1/a$ (14)	a=12.1, b=3.8, c=23.6, β=90.93, [010]		36-0102	5
	$WO_{2.8}$	Tetragonal P 4/n m m	a = 23.3, b = 23.3, c = 3.8, β = 90, [uvw not determined]		41-0475	
7.	WO_3	Tetragonal P -4 2_1 m (113)	a=7.390, b=7.390 , c=3.880 β=90, [001]	86144	89-1287	20
8.	$WO_{2.9}$	Tetragonal, P 4/n m m (129)	a=5.30(4) b=5.30(4) c=3.93(3), β=90, [110]	88367 WO_3	18-1417	14
9.	$WO_{2.9}$	Tetragonal, P 4/n m m (129)	a=5.30(4) b=5.30(4), c=3.93(3), β=90, [110]	88367	18-1417	6a
*A.	WO_3	Monoclinic, P $2_1/n$	a=7.30(2), b=7.53(3), c=7.69(3) β=90.78(3), various long directions	80056		This work
*B.	WO_3	Orthorhombic, P b a m	a=7.36(1) b=7.76(1) c=7.57(1), β=90, various long directions	50728		This work
*C.	WO_3	Tetragonal, P 4/n c c	a=5.28(6) b=5.28(6) c=7.84(1), β=90, various long directions	50733		This work

3.5. The state-of-the-art of the defect structure of WO_3

In a number of publications the synthesis of tungsten oxide nanorods was reported. It was not always reported clearly and correctly which phases were involved. Thus all different tungsten oxide phases with known structures were drawn from the ICSD (inorganic crystal structure database, FIZ Karlsruhe, edition 2011) of which a selection is listed in Table 2. The search yielded 64 entries for non-deficient WO_3 in 12 symmetrically different polymorphs with 11 different space groups. For oxygen deficient WO_{3-x} with subscript x ranging from 0.04 to 0.375 13 entries were described in 5 different space groups but 12 differently sized unit cells. The calculated patterns of all WO_3 phases and some of the WO_{3-x} phases are provided in Figure S1. The symmetries of the stable non-deficient polymorphs in air are with increasing temperature: P c (space group #7; T < 233 K) → P $\bar{1}$ (#2; 233 – 290 K) → (#14; 290 – 603 K) → P c n b (#62; 603 – 1013 K) → P 4/n c c (#130; 1013 – 1183 K) → P 4/n m m (#129; 1183 – 1503 K). For all

Revised Manuscript ID: CE-ART-03-2015-000526-R2

stable polymorphs there is no indication for oxygen-deficiency which is reasonable as W^{6+} being the preferred oxidation state of W and thus should not be reduced when heated in air. Locherer and Aird *et al.* reported [21] the reduction of WO_3 to tetragonal $WO_{2.9}$ (#113; P $\bar{4}$ 2_1 m; PDF 01-89-1287; ICSD 86144) by vapor deposition of Na metal on the surface of WO_3 single crystals at high temperature indicating difficult reduction of WO_3. As shown by these authors, tetragonal WO_{3-x} possesses much more distorted WO_6-octahedra than in WO_3. From the pattern of a well crystallized sample most polymorphs may easily be distinguished (see Fig. S1) and an unequivocal assignment of phases may be performed. An exception is in the distinction between the powder patterns of tetragonal WO_3 with space group P 4/n m m at high temperature and tetragonal $WO_{2.9}$ (P $\bar{4}$ 2_1 m) at room temperature, as only a few small extra reflections exist for the latter but not for the former. However, this distinction is most simple as only the latter one is observed at room temperature. Provided that the compositions of all database entries are reliable, it is thus also possible to distinguish between non-deficient and oxygen-deficient phases, which may be important as the physical properties strongly vary with composition.[22, 21(c)] In general it is stated that the observed succession of phases is clearly compatible with that of stable non-deficient WO_3.

3.6. DFT calculations of surface energies of WO_3 crystals.

In this section we aim at rationalizing the reasons for the observed growth of α–WO_3 crystals at high temperature on the basis of atomistic calculations based on Density Functional Theory (DFT). In doing this, we follow previous works, in which the ratio between surface energies of different crystal facets has been indicated as a driving force for the formation of strongly anisotropic crystal shapes or of crystalline nanowires [23] The relative stabilities of all low-pressure phases of bulk WO_3 at different temperatures have been computed by means of DFT techniques

Revised Manuscript ID: CE-ART-03-2015-000526-R2

in previous works. [24] With our simulation setup (see sections 2.3), the minimized cell parameters for monoclinic γ-WO_3 are: a=7.44 Å, b=7.60 Å, c=7.84 Å, β = 90.9°, the enthalpy of formation with respect to metallic W and gaseous O_2 is 9.0 eV (to be compared with the experimental value of 8.74 eV), [25] and the calculated cohesive energy is -4.67 eV per formula unit with respect to isolated gas-phase WO_3 molecules. For tetragonal α–WO_3 we obtain a=b=5.31 Å, c=7.91 Å and a cohesive energy of -4.63 eV. Taking into account that an overestimation of the computed cell parameters by about 1 to 2 % is typical for GGA exchange-correlation functionals, the matching between the computed and measured data is reasonably good and fully consistent with previous theoretical works. [24] Moreover, the computed cohesive energies are in agreement with the expected sequence of phase stability, the alpha phase lying 0.04 eV higher in energy than the gamma phase at 0 K (see Section 3).

We next compute the surface energies for various facets of the WO_3 nanocrystals, concentrating our attention on the γ and α phases. The effect of different oxygen terminations of the facets is taken into account within an ab-initio thermodynamics approach [26], in which the surface energy is written as

$$\gamma = E_{tot}(N_W N_O) - N_W E^{bulk}_{WO3} + (3 N_W - N_O) \mu_O, \qquad \text{Eq. (1)}$$

where $E_{tot}(N_W N_O)$ is the total energy of each surface model system containing N_W and N_O tungsten and oxygen atoms; E^{bulk}_{WO3} is the computed total energy of WO_3 for the respective bulk oxide phase, and μ_O is the oxygen chemical potential. The latter explicitly brings in a dependence of the surface energy on the temperature and the partial pressure p_{O2} of the oxygen gas which is assumed to be in equilibrium with the surface:

$$\mu_O(T,p_{O2}) = 1/2\,[E_{O2} + \mu^*_{O2}(T,p_0) + k_B T \ln(p_{O2}/p_0)]. \qquad \text{Eq. (2)}$$

Revised Manuscript ID: CE-ART-03-2015-000526-R2

Here, the chemical potential at the standard pressure p_0 (1 atm), $\mu^*_{O2}(T,p_0)$, includes the entropy of the oxygen gas and can be read from thermochemical tables, [25] and E_{O2} is the calculated total energy of a free oxygen molecule.

Tab. 3. Calculated surface energies (meV/Å^2) for low index surfaces of γ and α WO_3 at T=0 K. "O" and "WO" refer to 1.0 monolayer (ML) and 0.0 ML terminal O atoms, respectively.

Surface	Monoclinic		Tetragonal	
	O	WO	O	WO
100	93.48	101.97	139.19	220.14
010	106.55	111.67	140.36	218.58
001	115.07	112.09	103.57	101.95
110	149.24	217.48	89.32	118.35
101	153.55	201.06	139.95	244.74
011	161.69	210.11	111.64	244.07

The calculated surface energies at T = 0 K for low-index surfaces of the γ and α phases are listed in Tab. 3 for the extreme cases of oxygen-rich and oxygen-poor terminations ("O" and "WO", respectively, (Fig. 6).

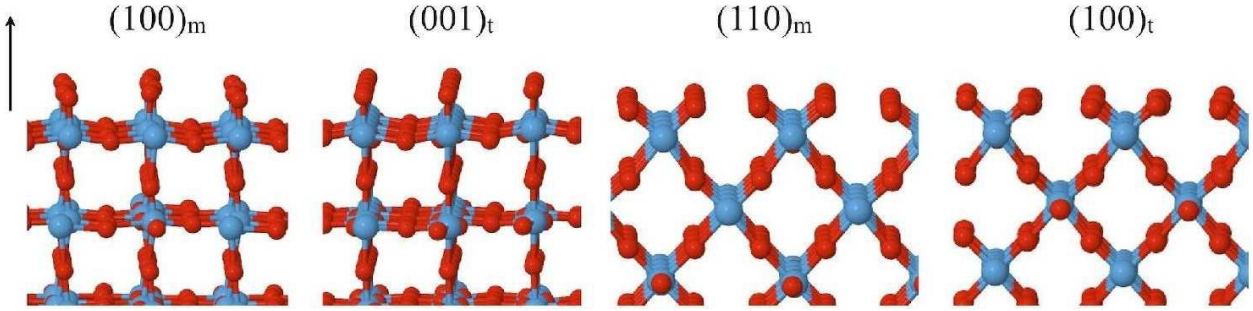

Fig. 6 Side view of selected, O-terminated surfaces of the monoclinic and tetragonal WO_3 crystals.

As a general trend, the lower surface energy values correspond to crystal truncations parallel to the central WO_4 planes of the WO_6 tetrahedra (basal surfaces), such as the $(100)_m$, $(001)_t$ or $(110)_t$ faces (see Section 3.3 and Fig. 6). Other truncations, such as $(110)_m$ or the crystallographic

Revised Manuscript ID: CE-ART-03-2015-000526-R2

equivalent $(100)_t$, are characterized by considerably higher surface energy values. The facets with lowest surface energy for the γ phase are indeed the one exposed by the nanoparticles at room temperature, as highlighted before in Section 3.2 (see Fig. 3). Since the α phase is only stable at high temperatures, a temperature-dependent analysis of the surface energies needs to be carried out before reaching conclusions about potentially preferential facets of tetragonal particles.

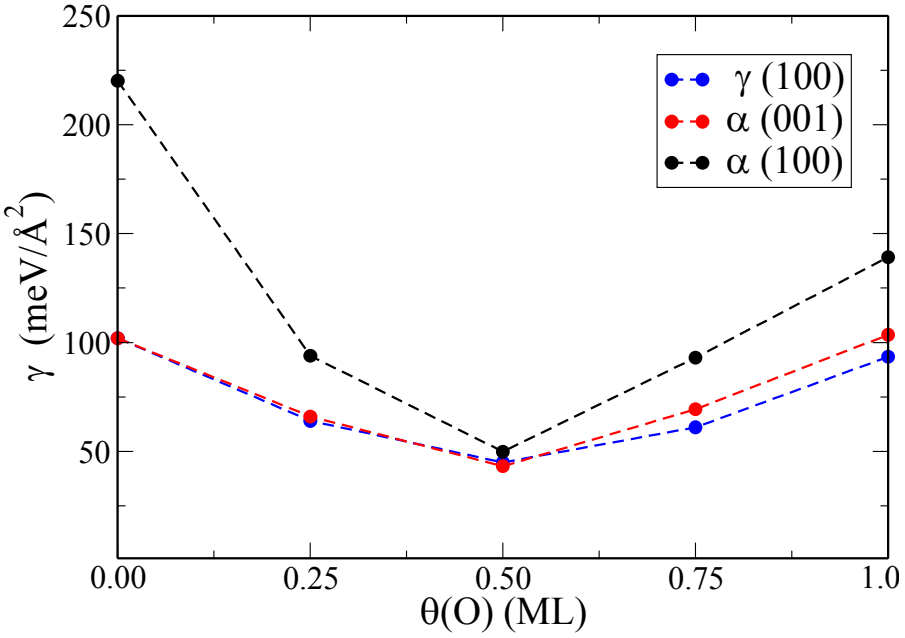

Fig. 7 Variation of the surface energy with the coverage of terminal O atoms for selected WO_3 surfaces.

In the following, we concentrate primarily on the $(100)_t$ and the $(001)_t$ facets as two representative examples.As already reported previously, the surface energy of WO_3 crystals is dominated by strong relaxations that arise from the polar nature of the surfaces. In particular, for non-stoichiometric, polar terminations, the excess or depletion of electronic charge may lead to surface metallicity. [27] Accordingly, we find that the coverage of terminal O atoms on each surface has a marked influence on the surface energy, which is lowest at a coverage of 0.5 monolayers (ML) both for the basal surfaces and for other surfaces such as $(100)_t$ (Fig. 7).

Revised Manuscript ID: CE-ART-03-2015-000526-R2

The densities of electronic states (DOS) for the case of 0.5 ML of O (stoichiometric termination) and 0.0 ML of O (oxygen depletion) are shown exemplarily for the $(001)_t$ surface in Fig. 8. As expected, the metallicity and the consequent higher reactivity of the latter case is visible from the absence of a clear band gap with the Fermi Level crossing the valence band. In the former case, only a small peak corresponding to a surface state pinning the Fermi level is visible before the band gap.

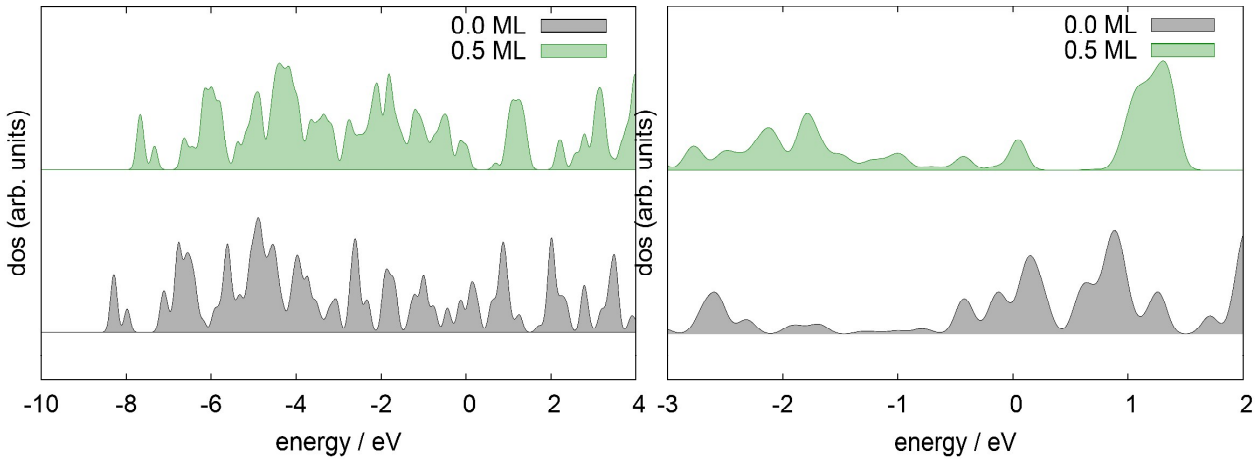

Fig. 8 Densities of states (DOS) of the (001) alpha-WO_3 surface for the case of stoichiometric termination (0.5 ML of O) and oxygen depletion (0.0 ML of O), shown in green and black, respectively. The Fermi level is set to 0 eV in both cases. Left: global DOS of the entire slab model including the whole valence band. Right: local DOS projected on the surface W atoms in an energy window close to the Fermi level.

The relative stability of different oxygen surface terminations is strongly dependent on the temperature and partial pressure of oxygen gas, according to Equations (1) and (2). The computed surface energies as a function of temperature for the case of atmospheric (0.1 atm) and experimental vacuum conditions (10^{-6} atm) are reported in Fig. 9 for the $(001)_t$ and $(100)_t$ surfaces of the high-temperature α phase (the behaviour of $(100)_m$ does not differ from the one of $(001)_t$, due to the crystallographic equivalence of the two surfaces and the resulting negligible differences of surface energy at 0K shown in Fig. 7).

Revised Manuscript ID: CE-ART-03-2015-000526-R2

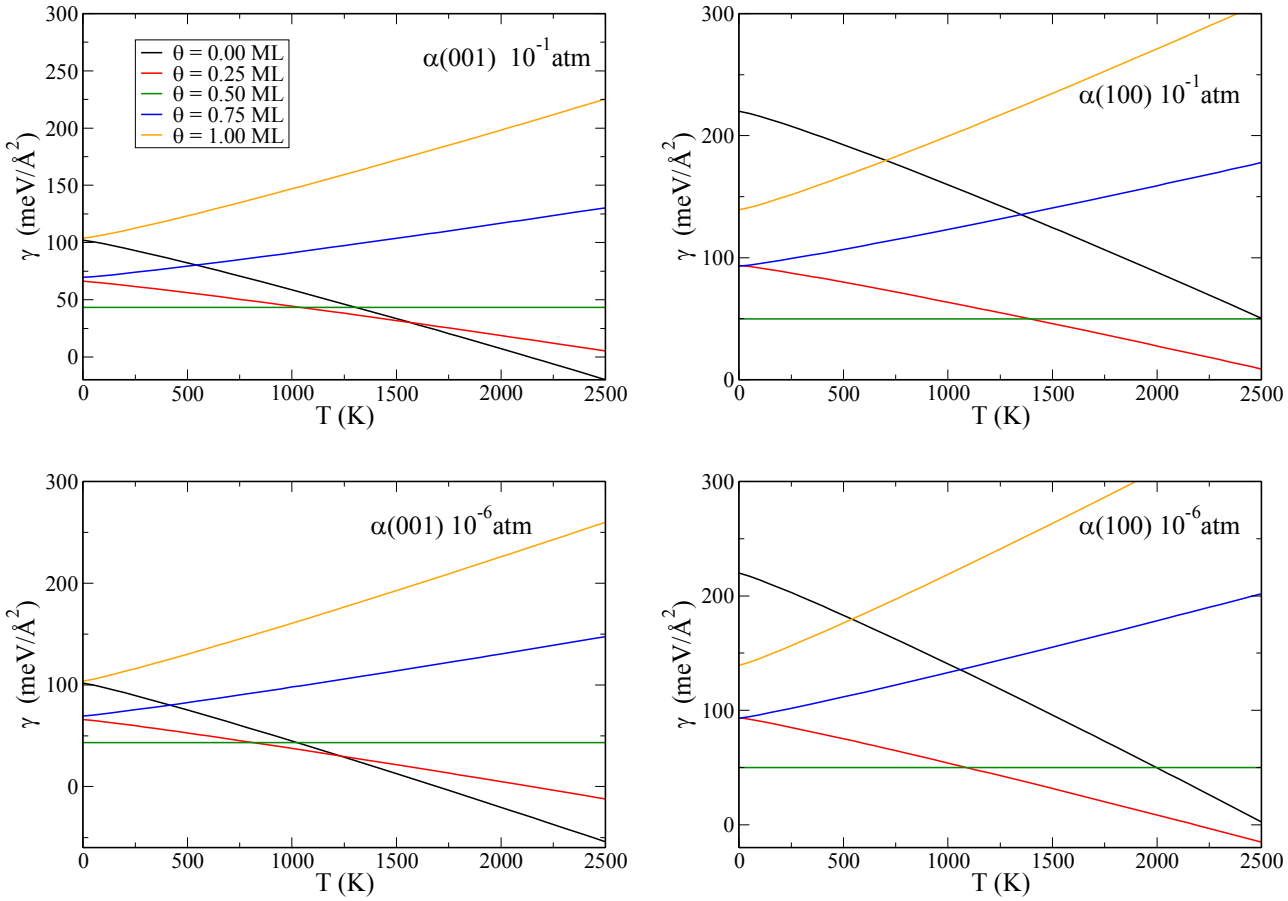

Fig. 9 Variation of the surface energies versus temperature for the (001)t and (100)t surfaces at ambient and vacuum oxygen pressures, for different oxygen terminations.

In the low-temperature regime, the stoichiometric, non-polar termination (0.5 ML O coverage) is clearly favored for both surfaces. Oxygen desorption is expected to take place at temperatures close to the phase boundary between the orthorhombic and the tetragonal phases (~730°C), especially if the surface is exposed to low partial O pressure, as in the high-vacuum TEM chamber. At the temperature in which the formation of larger particles is observed within the TEM (see Fig. 3 and 5 in Section 3.2), i.e. ~930°C, the surface energies of the (001) and (100) facets are about 30 and 45 meV/Å^2, respectively, indicating a slight thermodynamic preference for the formation of elongated particles along the (100) direction, as indeed observed for the

Revised Manuscript ID: CE-ART-03-2015-000526-R2

some of our crystals, and in particular for those presenting the largest aspect ratios (Fig. 3g,h and 5a).

3.7. First-principles MD simulations of elongated crystal growth

Dynamical simulations of WO_3 growth are carried out through consecutive first principles molecular dynamics (FPMD) simulations of the interaction of WO_3 molecules with the (001) and (100) surfaces of α-WO_3. In each simulation, two WO_3 molecules, initially at rest, are placed at a distance of about 2 to 3 Å (distance of the W atoms from the surface) over the fully relaxed surface, i.e. at virtually 0 K, and the system is set free to evolve according to a microcanonical CP dynamics for about 2 ps. After that, the temperature of the simulation is increased to about 900 K over about 200 fs, and the dynamical evolution of the system is simulated for further 3 ps on average, before quenching the atomic motion to complete relaxation.

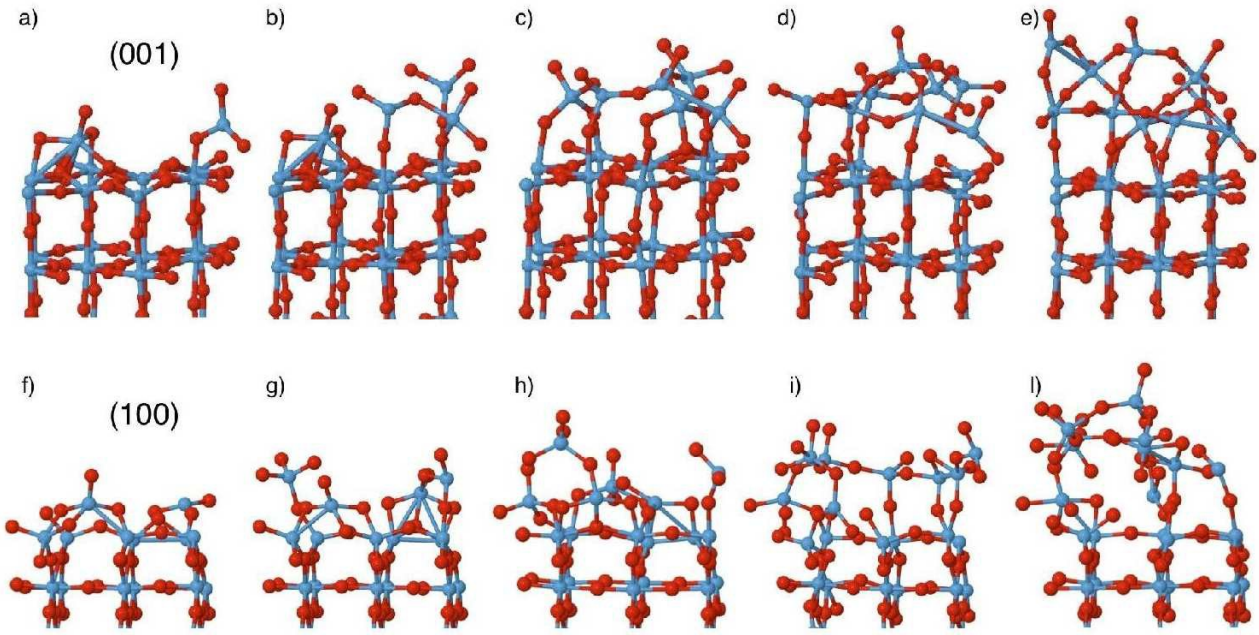

Fig. 10 Adsorption of WO_3 molecules on the α-WO_3(001) surface. W atoms are shown in blue, O atoms in red. Going from panel a) to e), 2 WO_3 molecules have been added each time and dynamical FPMD simulations have been performed. Periodic boundary conditions are applied.

Revised Manuscript ID: CE-ART-03-2015-000526-R2

Starting with the bare (001) surface and no terminal oxygen, the first two molecules approach the surface with formation of new W-O bonds while they retain their molecular geometry, as shown in Fig. 10 a). The further two WO_3 molecules adsorb without modifying significantly the existing structure, arranging preferentially in a four-fold, tetrahedron-like oxygen coordination shell (Fig. 10 b). During the subsequent adsorption of a fifth and sixth WO_3 molecules (Fig. 10 c), the first atomic layer arranging on the α-WO_3(001) surface clearly evolves into a layer of merely oxygen atoms, bound to the W atoms of the original surface layer. On the contrary, the incoming W atoms do not form any new bond with the O atoms of the surface layer, but remain above the newly formed oxygen layer. During further molecule absorption and growth [Fig. 10 d-e), the first layer of oxygen is preserved, showing a regular arrangement of the O atoms on top of the W atoms of the surface. After the adsorption of ten WO_3 molecules, a fully intact first layer of oxygen atoms covers the original surface layer, suggesting an epitaxial growth of the octahedral lattice structure. Here, the term "epitaxial" is used to indicate that the mere deposition process of novel WO_3 molecule immediately leads to a new layer possessing the symmetry of the underlying surface, without the need for atomic re-arrangements taking place on a time-scale not accessible by our simulations.

A similar behavior is observed in the simulations of WO_3 adsorption over the (100) surface (Fig. 10 f-l). However, the arrangement of the molecules obtained after formation of a novel layer over the surface is more disordered than for the previous orientation [compare Fig. 10l with Fig. 10e). For both orientations, the average W-O bond length in the new layer is about 1.95 Å, which is closer to the average bulk bond length of α-WO_3 (1.93 Å) than the W-O bond length of an isolated WO_3 molecule (1.75 Å). The W atoms of the incoming molecules, reallocating in a W/O network above the first oxygen layer, progressively increase their coordination number, and a first W atom arranging in an octahedral lattice position can be observed over the (001) surface at

Revised Manuscript ID: CE-ART-03-2015-000526-R2

the maximum coverage investigated. The computed Bader atomic charges on the W atoms in the newly formed W/O networks are in the range 2.5 – 3.0 electrons, thus lying between the charge of W in the isolated WO_3 molecule (2.5 e) and the WO_3 bulk value (3.2 e).

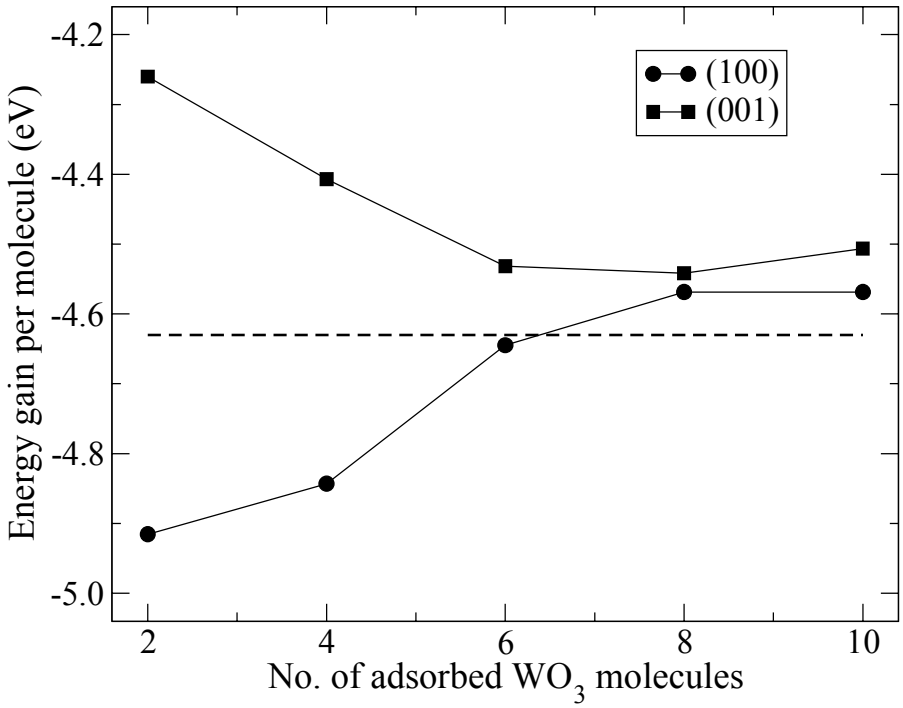

Fig. 11 Energetic gain calculated during the growth of an α-WO_3 crystal exposing (100) and (001) facets. The gained energy is averaged of the total number of newly adsorbed WO_3 and reported as a function of their number. The dashed line marks the value of cohesive energy of bulk α-WO_3 (-4.63 eV).

In Fig. 11, we report the energetic gain per molecule averaged over the total number of newly adsorbed WO_3 molecules as a function of their number. Interestingly, at the largest coverages the gained energy converges to roughly the same value for both orientations (about -4.55 eV), which is only slightly smaller than the cohesive energy of the tetragonal crystal (-4.63 eV/molecule). However, at low coverages the gained energy is *deeper* than the cohesive energy for the (100) orientation, while it is evidently *higher* for the (001) orientation. From these results we can conclude that the growth of a pre-existent crystal of α-WO_3 exposing (001) and (100) facets upon molecular deposition from the gas phase is expected to proceed more favorably along the (100)

Revised Manuscript ID: CE-ART-03-2015-000526-R2

orientation, which matches the experimentally observed direction of growth of the elongated particles in Fig. 3g,h and Fig. 5a. Despite the limited time accessible to our FPMD simulation, and thus the impossibility of forming a perfectly ordered crystalline structure of the novel layer, the growth seems to proceed almost epitaxially over the (001) surface, while a more disordered layer initially develops along the faster direction of growth, (100).

4. Discussion

4.1. Crystallographic and morphological transitions of WO_3 nanoparticles

Flame Spray Pyrolysis is a versatile tool to produce oxide nanoparticles with variable composition and crystallographic ordering. Depending on the specific process conditions and on the synthesized material, it is possible to obtain either phases in thermodynamical equilibrium or metastable phases after rapid quenching of the products formed in the flame to room temperature upon collection on suitable substrates. Regarding WO_3, the processing temperature in the flame (about 2000 K) would be consistent with the formation of the tetragonal α phase. However, the particles collected at room temperature clearly exhibit monoclinic symmetry (see Figs. 2a and 3a). In light of the results presented in this work, such finding can be rationalized in terms of an α–β–γ phase transformation that takes place rapidly enough during the cooling process. In fact, the possibility of a first-order α–β and a second-order β–γ phase transition as a consequence of changes in the WO_6 tetrahedral tilt system in the crystal has been suggested.[8]

Our results indeed confirm that both transitions take place reversibly in a heating/cooling cycle starting from as-synthesized γ-WO_3 nanoparticles. However they indicate that the mechanism of the β–α transition differs substantially depending on the direction of the temperature gradient. Namely, an evaporation/reprecipitation process occurs during heating, leading to an evident enlargement of α-WO_3 particles, which in some cases appear to be elongated with aspect ratios of

Revised Manuscript ID: CE-ART-03-2015-000526-R2

about 3:1. Instead, only a re-arrangement of the tetrahedral tilts takes place during cooling, preserving the habitus of the elongated particles previously produced.

Therefore, while the crystallographic phase transitions are reversible along the cycle, the associated morphological transitions are not. Notably, a direct growth of monoclinic elongated particles is impeded by the very similar values of the surface energies of the exposed nanocrystal facets (see Tab. 4), which correspond to the principal direction of the monoclinic unit cell, (100), (010), (001) as visible in the TEM and SAED analysis presented in Fig. 3b.

4.2. Growth of WO_3 particles at high temperature

When WO_3 nanoparticles are heated, our in-situ TEM analyses first show a slight enlargement of the average particle size (at intermediate temperatures) and later the formation of some elongated particles due to particle-particle aggregation as well as evaporation/re-precipitation (see Fig. 3 and 5). In fact, sublimation of the WO_3 crystals to WO_3 molecules at temperatures well below the melting point (1746 K {, 2009 #234}) has been reported before in a number of previous studies [15, 17-18, 28]. This is consistent with the fact that our calculated surface energies for the $(001)_t$ and $(100)_t$ surfaces decay rapidly at temperatures higher than about 1000 and 1400 K at atmospheric O pressure, respectively. At very low O pressure, these temperatures are reduced to about 800 and 1100 K, respectively.

Unfortunately, the strong approximations inherent in our calculations (for instance, neither zeropoint energy corrections, nor entropic differences of the surfaces at different temperatures and O terminations are considered) do not allow us to draw a quantitative comparison between calculations and experiments. Moreover, we note that our modeling analysis mainly concerns the thermodynamic driving forces for the formation of particles with a highly anisotropic aspect ratio. Kinetic effects, which are also expected to govern the formation of elongated particles or

Revised Manuscript ID: CE-ART-03-2015-000526-R2

nanowires, are not considered here, with the exception of the short-time-scale MD simulations. However, the deposition of gas-phase WO_3 molecules at high temperatures is not expected to be associated with any adsorption energy barrier, so that the potential energy gain after adsorption and the equilibrium surface energies do indeed represent good indicators for the (relative) reactivity, and thus for the growth speed, of different crystal facets. For this reason we have limited ourselves to modeling of only two facets of the tetragonal phase. However, it is interesting to note that the overall smaller absolute values of surface energy at any given temperature are obtained for the $(001)_t$ facet, and that a slightly larger values is associated with the $(100)_t$ facet. These results thus suggest that accretion of WO_3 crystals via deposition of WO_3 molecules from the gas phase could proceed preferentially along the $(100)_t$ direction under growth conditions close to thermodynamical equilibrium. A further support of possible preferential growth along the $(100)_t$ direction is provided by the results of FPMD simulations.

5. Conclusion

We have found that the deposition of gaseous WO_3 proceeds spontaneously on the surface of a pre-existing crystal irrespective of the facet orientation, consistently with the enlargement of the nanoparticles in both directions observed in the in-situ TEM experiments. However, the energy gain associated with the deposition of new molecules from the gas phase is clearly favored for the $(100)_t$ direction, presenting values even deeper than the cohesive energy of the crystal. Therefore, under the high-temperature conditions leading to evaporation and reprecipitation, we can expect a faster accretion of the latter with respect to the $(001)_t$ facet. We note that the relatively small differences between the surface energies of different facets, the possible occurrence of surface reconstructions during the particle growth, and competitive growth mechanism such as particle-particle agglomeration can also lead to slightly elongated particles along other directions, as

Revised Manuscript ID: CE-ART-03-2015-000526-R2

observed for instance in Fig. 5(b,c). Taken together, our XRD, in-situ TEM and DFT results explain the formation of elongated tungsten trioxide particles upon the heating of nanoparticles in terms of a complex driving force arising both from different surface stability and different reactivity towards gas-phase deposition of molecular WO_3.

Acknowledgments

SP and LM would like to acknowledge the funding from US Public Health Service Grants, U19 ES019528 (UCLA Center for Nanobiology and Predictive Toxicology) and RO1 ES016746, the National Science Foundation and the Environmental Protection Agency under Cooperative Agreement Number DBI 0830117 and 1266377. Allocation of computer time has been provided by the University of Bremen, the HLRN supercomputing centre (Hannover-Berlin) and the ZIH supercomputing centre (Dresden). We acknowledge funding via the APF programme "Func-Band" of the Land Bremen.

Supporting information available: The inorganic crystal structure database (ICSD, FIZ Karlsruhe) entries for deficient and non-deficient WO_3 in various symmetrically different polymorphs and different space groups are included (1 word and 1 excel files). The Bremen Rietveld Analysis and Structure Suit, **2009**, unpublished beta version can be obtained from author Johannes Birkenstock, Fachbereich Geowissenschaften, Universität Bremen, Official version **2007**, http://www.brass.uni-bremen.de/

References

1 (a) G. Hodes, D. Cahen, J. Manassen, *Nature* 1976, **260**, 312; (b) S. H. Lee, R. Deshpande, P. A. Parilla, K. M. Jones, B. To, A. H. Mahan, A. C. Dillon, *Advanced Materials* 2006, **18**, 763; (c) J. Rajeswari, P. Kishore, B. Viswanathan, T. Varadarajan, *Nanoscale Res. Lett.* 2007, **2**, 496; (d) A. Tiwari, S. Li, *Polym. J.,* 2009, **41**, 726; (e) L. Wang, L. A. Teleki, S. E.

Revised Manuscript ID: CE-ART-03-2015-000526-R2

Pratsinis, P. I. Gouma, P. I. *Chem. Mater.,* 2008, **20,** 4794; (f) M. Wang, G. Fang, L. Yuan, H. Huang, Z. Sun, N. Liu, S. Xia, X. Zhao, *Nanotechnol.,* 2009, **20**, 185304.

2 (a) S. Pokhrel, A. E. Nel, L. Mädler, Acc. Chem. Res. 2012, **46**, 632; (b) J. A. Kemmler, S. Pokhrel, L. Mädler, U. Weimar, N. Bârsan, *Nanotechnology*, 2013, **24**, 442001; (c) J. A. Kemmler, S. Pokhrel, J. Birkenstock, M. Schowalter, A. Rosenauer, N. Bârsan, U. Weimar, L. Mädler, *Sens. Actuators B: Chem.*, 2012, **161**, 740;(d) W.Y. Teoh, R. Amal, L. Mädler, *Nanoscale*, 2010, **2**, 1324; (e) S. Pokhrel, J. Birkenstock, M. Schowalter, A. Rosenauer, L. Mädler, *Crystal Growth & Design* 2009, **10**, 632; (f) S. Pokhrel, C. E. Simion, V. S. Teodorescu, N. Bârsan, U. Weimar, *Adv. Funct. Mater.,*2009, **19**, 1767; (g) P. Yang, D. Zhao, D. I. Margolese, B. F. Chmelka, G. D. Stucky, *Nature,* 1998, **396**, 152; (h) N. Pinna, M. Niederberger, *Angew. Chem. Int. Ed.* 2008, **47**, 5292; (i) J. Polleux, A. Gurlo, N. Barsan, U. Weimar, M. Antonietti, M. Niederberger, *Angew. Chem. Int. Ed.,* 2006, **45**, 261; (j) B. C. Satishkumar, A. Govindaraj, M. Nath, C. N. R. Rao, *J. Mater. Chem.*, 2000, **10**, 2115; (k) K. Lee, W. S. Seo, J. T. Park, *J. Am. Chem. Soc.*, 2003, **125**, 3408; (l) Y. Baek, Y. Song, K. Yong, *Adv. Mater.,* 2006, **18**, 3105; (m) C. Klinke, J. B. Hannon, L. Gignac, K. Reuter, P. Avouris, *J. Phys. Chem. B*, 2005, **109**, 17787; (n) Z. Gu, T. Zhai, B. Gao, X. Sheng, Y. Wang, H. Fu, Y. Ma, J. Yao, *J. Phys. Chem. B*, 2006, **110**, 23829; (o) X. W. Lou, H. C. Zeng, *Inorg. Chem.,* 2003, **42**, 6169.

3 (a) J. Wang, E. Khoo, P. S. Lee, J. Ma, *J. Phys. Chem. C*, 2008, **112**, 14306; (b) J. Wang, E. Khoo, P. Lee, J. Ma, J. *J. Phys. Chem. C*, 2009, **113**, 9655.

4 (a) T. Maiyalagan, B. Viswanathan, *J. Power Sources*, 2008, **175**, 789; (b) W. Smith, Z. Y. Zhang, Y. P. Zhao, *J. Vacuum Sci. Technol. B: Microelectr. Nano Structur.*, 2007, **25**, 1875; (c)Y. He, Y. Zhao, Y. *Nanoscale*, **2011**, *3*, 2361.

5 J. Thangala, S. Vaddiraju, R. Bogale, R. Thurman, T. Powers, B. Deb, M. K. Sunkara, *Small*, 2007, **3**, 890.

6 (a) J. F. Al-Sharab, R. K. Sadangi, V. Shukla, S. D. Tse, B. H. Kear, *Cryst. Growth & Design*, 2009, **9**, 4680; (b) Y. Baek, K. J. Yong, *Phys. Chem. C*, 2007, 111, 1213; (c) R. Hu, H. Wu, K. Hong, *J. Cryst. Growth*, 2007, **306**, 395.

7 C. V. Ramana, S. Utsunomiya, R. C. Ewing, C. M. Julien, U. Becker, *Physica status solidi (a)* **2005**, *202*, R108.

8 T. Vogt, P. M. Woodward, B. A. Hunter, *J. Solid state Chem*. **1999**, 144, 209.

9 R. Schlitzer, *Ocean Data View* 2009, *http://odv.awi.de*.

10 J. Birkenstock, R. X. Fischer, T. Messner, *The Bremen Rietveld Analysis and Structure Suite* 2011.

11 (a) A. G. S. Filho, J. M. Filho, V. N. Freire, A. P. Ayala, J. M. Sasaki, P. T.C. Freire, F. E. A. Melo, J. F. Julião, U. U. Gomes, *J. Raman Spectr.,* 2001, **32**, 695; (b) K. R. Locherer, I. P. Swainson, E. K. H. Salje, *J Phys.: Cond. Matter***,** 1999, **11**, 6737; (c) E. Salje, K. Viswanathan, *Acta Crystallogr. A*, 1975, **31**, 356.

12 E. Salje, *Acta Crystallogr. B*, 1977, **33**, 574.

13 C.-Y. Su, H. -C Lin, T.-K. Yang, C.-C. Chang, C.-K. Lin, *Mater. Trans.,*2009, **50**, 2593.

14 Y. M. Zhao, Y. H. Li, I. Ahmad, D. G. McCartney, Y. Q. Zhu, W. B. Hu, *Appl. Phys. Lett.*, 2006, **89**, 133116.

15 C.-Y. Su, H.-C. Lin, T.-K. Yang, C.-K. Lin, *J. Nanopart. Res.* 2009*,* **12**, 1755.

16 B. Mwakikunga, E. Sideras-Haddad, C. Arendse, M. Witcomb, A. Forbes, A. *J. Nanosci. Nanotechnol.*, 2009, **9**, 3286.

17 L. Di, L. Bo, O. Akihisa, N. Masaaki, *J. Vacuum Sci. & Technol. B,* 2010*,* **28**, C2A98.

18 F. C. Cheong, B. Varghese, Y. Zhu, E. P. S. Tan, L. Dai, V. B. C. Tan, C. T. Lim, C. H. Sow, *J. Phys. Chem. C,* 2007, **111**, 17193.

Revised Manuscript ID: CE-ART-03-2015-000526-R2

19 Y. Zhang, Y. Chen, H. Liu, Y. Zhou, R. Li, M. Cai, X. Sun, *J. Phys. Chem. C*, 2009, **113**, 1746.

20 W. Wu, Q. Yu, J. Lian, J. Bao, Z. Liu, S.-S. Pei, *J. Cryst. Growth*, 2010, **312**, 3147-3150.

21 (a) A. Aird, E. K. H. Salje, *J. Phys: Condensed matter*, 1998, **10**, L377; (b) A. Aird, M. C. Domeneghetti, F. Mazzi, V. Tazzoli, E. K. H. Salje*, J. Phys: Condensed matter*, 1998, **10**, L569; (c) K. R. Locherer, I. P. Swainson, E. K. H. Salje, *J. Phys.: Cond. Matter*, 1999, **11**, 4143.

22 K. R. Locherer, I. P. Swainson, E. K. H. Salje, *J. Phys.: Cond. Matter***,** 1999, **11**, 6737.

23 (a) A. Beltrán, J. Andrés, E. Longo and E. R. Leite, *Appl. Phys. Lett*., 2003, **83**, 635; (b) S. Sakong, Y. A. Du, P. Kratzer, *Phys. Rev. B* 2013, 88, 155309; (c) S.-M. Ko, J.-H. Kim, Y.-H. Ko, Y. H. Chang, Y.-H. Kim, J. Yoon, J. Y. Lee, Y.-H. Cho, *Crystal Growth & Design* 2012, 12, 3838

24 (a) R. Chatten, A. V. Chadwick, A. Rougier, P. J. D. Lindan, *J. Phys. Chem. B*, 2005, **109**, 3146; (b) A. D. Walkingshaw, N. A. Spaldin, E. Artacho, *Phys. Rev. B*, 2004, **70**, 165110.

25 CRC Handbook of Chemistry and Physics, 90th Edition, CRC Press, Boca Raton, 2009.

26 K. Reuter, M. Scheffler, *Phys. Rev. B*, 2001, **65**, 035406.

27 (a) M. Stengel, *Phys. Rev. B*, 2011, **84**, 205432; (b) I. N. Yakovkin, M. Gutowski, *Surf. Sci*, 2007, **601**, 1481.

28 Y. M. Zhao, Y. H. Li, I. Ahmad, D. G. McCartney, Y. Q. Zhu, W. B. Hu, *Appl. Phys. Lett.* 2006, **89**, 133116 (1-3).

Revised Manuscript ID: CE-ART-03-2015-000526-R2

Table of contents (TOC): The structural transformation of WO_3 at high temperatures